



NOMATEN

This work was carried out in whole or in part within the framework of the NOMATEN Centre of Excellence, supported from the European Union Horizon 2020 research and innovation program (Grant Agreement No. 857470) and from the European Regional Development Fund via the Foundation for Polish Science International Research Agenda PLUS program (Grant No. MAB PLUS/2018/8), and the Ministry of Science and Higher Education's initiative "Support for the Activities of Centers of Excellence Established in Poland under the Horizon 2020 Program" (agreement no. MEiN/2023/DIR/3795).

The version of record of this article, first published in *Journal of Alloys and Compounds*, Volume 1035, 5 July 2025, 181580, is available online at Publisher's website:
<https://doi.org/10.1016/j.jallcom.2025.181580>

This manuscript version is made available under the CC-BY-NC-ND 4.0 license.

Exploring the impact of Ti/Al on L₁₂ nanoprecipitation and deformation behavior in CoNiFeAlTi multi-principal element alloys through atomistic simulations

Amin Esfandiarpour^{1*}, Anshul D. S. Parmar¹, Silvia Bonfanti¹, Pawel Sobkowicz¹, Byeong-Joo Lee^{2*} and Mikko Alava^{1,3}

¹ NOMATEN Centre of Excellence, National Centre for Nuclear Research, Otwock, Andrzej Soltana 7, 05-400, Poland

² Department of Materials Science and Engineering, Pohang University of Science and Technology, Pohang 37673, South Korea

³ Department of Applied Physics, Aalto University, P.O. Box 11000, 00076 Aalto, Espoo, Finland

* Corresponding authors amin.esfandiarpour@ncbj.gov.pl (Amin Esfandiarpour) and calphad@postech.ac.kr (Byeong-Joo Lee)

Abstract

Recent experimental studies on CoNi-based multi-principal element alloys (MPEAs) have demonstrated high strength and ductility, attributed to the formation of stable L₁₂ nanoscale precipitates. However, the fundamental mechanisms behind such impressive properties in these complex alloys are not well understood. In this work, we investigate the effects of Ti and Al concentrations on the formation of L₁₂ precipitates in (CoNiFe)₈₄(Al₈Ti₈), (CoNiFe)₈₆(Al₇Ti₇), (CoNiFe)₈₈(Al₆Ti₆), and (CoNiFe)₉₄(Al₄Ti₂) MPEAs using hybrid molecular dynamics/Monte Carlo (MD/MC) simulations and a developed MEAM interatomic potential for the CoNiFeTiAl system. Additionally, we study the effect of L₁₂ precipitation on the mechanical properties and stacking fault energy of these MPEAs using MD. Our hybrid MD/MC simulations show that (CoNiFe)₈₆(Al₇Ti₇) alloy exhibits the highest amount of L₁₂ nanoprecipitates. We find that L₁₂ precipitation increases the stacking fault energy, with higher Al and Ti contents leading to greater increases. Tensile simulations reveal that L₁₂ precipitates enhance yield strength, with alloys exhibiting higher precipitation showing increased flow stress. We also investigate dislocation-nanoprecipitate interactions with different precipitate sizes in (CoNiFe)₈₆(Al₇Ti₇) alloy. Larger nanoprecipitate sizes result in stronger dislocation pinning. Dislocation-precipitate interactions indicate that dislocations predominantly shear through 4-8 nm precipitates instead of looping around them (Orowan mechanism), which enhances strength while maintaining good ductility. Although the lattice mismatch between the L₁₂ nanoprecipitate and the matrix is low (0.139%), the significant difference in stacking fault energy between the L₁₂ nanoprecipitate and the matrix results in stronger dislocation pinning. This fundamental understanding can guide the compositional design of MPEAs with tailored properties by controlling nanoscale precipitation.

Keywords: L₁₂ nanoprecipitates, Hybrid MD/MC, SFE mismatch, strength-ductility trade-off, multi-principal element alloys

1. Introduction

The development of multi-principal element alloys (MPEAs), also known as high- or medium-entropy alloys (HEAs/MEAs), presents significant opportunities for materials innovation. These alloys exhibit superior physical and mechanical properties compared to conventional alloys, making

them promising candidates for future structural applications [1]. However, designing MPEAs with desirable mechanical properties faces considerable challenges due to their vast composition space [2,3]. A primary challenge is the trade-off between strength and ductility in HEAs/MEAs, which complicates the design of novel MPEAs [4]. For example, HEAs/MEAs with a body-centered cubic (BCC) structure exhibit high strength at elevated temperatures but low ductility at room temperature [5]. Conversely, face-centered cubic (FCC) H/MEAs demonstrate good ductility but lower strength at high temperatures [6].

Numerous strategies for designing strong MPEAs with good ductility have been presented. For instance, some dual-phase FCC-BCC MPEAs effectively balance both ductility and strength [7–10]. Due to the high ductility of FCC-MPEAs, one strategy to enhance strong-ductile MPEAs is to increase the strength of FCC-MPEAs through solid solution strengthening. Following this strategy, FCC-MPEAs with three constituent elements exhibit higher lattice distortion and strength compared to quaternary and quinary MPEAs [11–16]. Complementary to such designs, short-range order (SRO) strengthening can also be employed to increase their strength [17–21]. Additionally, nanoprecipitates (NPs) can further improve the mechanical properties of these materials [22–24]. The size and volume fraction of precipitates significantly affect both ductility and strength, with nano-sized precipitates in MPEAs overcoming the strength-ductility trade-off [22,25–27]. Specifically, L_{12} NPs can form in some FCC-MPEAs by adding Al and Ti [25,28–36], resulting in alloys with high strength and good ductility. Stacking fault energy (SFE) also plays a crucial role in the mechanical properties of these alloys [25,29,37]. Despite numerous recent experimental studies, a fundamental understanding of the formation of such precipitates and their effect on the mechanical properties of these complex alloys remains lacking.

In this study, we construct a MEAM interatomic potential for CoNiFeTiAl to investigate how varying atomic percentages of Al and Ti influence the formation of the L_{12} phase in several CoNiFeAlTi alloys, using a hybrid molecular dynamics/Monte Carlo (MD/MC) method. Hybrid MD/MC is a widely used method to investigate the ordering phase after annealing in High/Medium Entropy Alloys (H/MEAs) [13,17,18,38–41]. For instance, SRO in CoNiCr, as observed in experimental studies [42], was detected using this method [17,18,39]. Furthermore, the formation of the L_{12} phase ordering was studied in Fe_xNi_{1-x} alloys with hybrid MD/MC [41], yielding results consistent with experimental findings [43]. We performed tensile tests to investigate the effect of NPs on yield strength and flow stress. Using molecular statics, we examined the dependency of SFE on Al and Ti concentrations. Additionally, we investigated the dependency of SFE on the concentration of L_{12} . Finally, using shear control loading, we examined the effect of L_{12} NPs on dislocation pinning.

2. Methods

All molecular dynamics (MD) simulations conducted in this study utilized the large-scale atomic/molecular massively parallel simulator (LAMMPS) [44]. In this study, all simulations employed the second nearest-neighbor modified embedded atom method (2NN MEAM) interatomic potential. Modeling the CoNiFeAlTi quinary system required potential parameter sets for the constituent unary, binary, and ternary systems. Published potentials were used for the pure elements (Co [45], Ni [45], Fe [46], Al [47], Ti [48]) as well as the binary pairs (Co-Fe [49], Co-Ni [50], Co-Al [50], Co-Ti [51], Ni-Fe [52], Ni-Al [53], Ni-Ti [53], Fe-Al [54], Fe-Ti [55], Al-Ti [53]). Ternary potentials for Co-Ni-Fe [49], Co-Ni-Al [50], Ni-Fe-Al [56], and Ni-Al-Ti [53] systems were also available from prior works. However, potentials for the remaining ternary combinations had not been previously developed. We derived the missing potential parameters using an approach analogous to Choi et al [49]. Modeling each ternary system involved determining six screening parameters: three $C_{min}(i-j-k)$ and three $C_{max}(i-j-k)$ values. These parameters describe the

screening effect of an atom j on the interactions between neighboring atoms i and k . The screening parameters were assigned values based on an averaging concept. We listed all these parameters for the ternary systems in Table S1. With all required potentials determined, the complete quinary interatomic potential was obtained. The parameter values for this potential in LAMMPS format are provided as supplementary information. In addition, to validate this potential, the elastic constant and stacking fault energy of the $(\text{Ni,Co,Fe})_3(\text{Ti,Al,Fe})$ L_{12} phase that formed in $(\text{CoNiFe})_{86}(\text{Al}_7\text{Ti}_7)$ alloy were compared with results obtained using density functional theory (DFT) method [57] (see Table S2). The results show good agreement between the MEAM and DFT data.

To investigate the effect of Al and Ti on L_{12} phase formation in CoNiFeAlTi alloys, we conducted hybrid MD/MC atomistic simulations at temperature 300 K and 1100 K. The simulations followed the hybrid MD/MC approach described in Refs. [4,5]. Initially, Co, Ni, Fe, Al and Ti atoms were randomly distributed in a FCC simulation box with dimensions of 110.49 Å along $\langle 100 \rangle$, 242.36 Å along $\langle 010 \rangle$, and 114.05 Å along $\langle 001 \rangle$, which was then exposed to energy minimization via the conjugate gradient method. The system was equilibrated at the target temperature under NPT ensemble conditions. The subsequent MC swap methodology involved randomly selecting two atoms of different elemental types and attempting to swap their identities while conserving the total kinetic energy. The acceptance criterion for each attempted swap move followed the Metropolis probability: $u \leq \min(1, \exp[-\beta\Delta U])$, where u is a uniform random number between 0 and 1, ΔU is the potential energy change from the swap, $\beta = 1/k_B$, and k_B is the Boltzmann constant. Following a sequence of 200 swap attempts, the system was relaxed for 50 molecular dynamics steps under NPT conditions. This cycle of swap attempts and relaxations continued iteratively until the system's potential energy satisfactorily converged. A total of 14 million swap attempts were made. To analyze the ordering type, we calculated the total percentage of L_{12} atoms using the polyhedral template matching method [58]. We considered the Al and Ti atoms as the first group and the Co, Ni, and Fe atoms as the second group. The total L_{12} atoms were then extracted based on this grouping.

To see the effect of L_{12} on the tensile properties and SFE, we created FCC samples with the orientation $X = [1\bar{1}2]$, $Y = [\bar{1}11]$, and $Z = [\bar{1}\bar{1}0]$, containing 55296 atoms with approximate dimensions $69.6 \times 147.6 \times 60.3 \text{ \AA}^3$.

We conducted uniaxial tensile tests using MD both before and after hybrid MD/MC simulations in the y direction. The NPT ensemble was employed during the deformation process, with the pressure in the direction perpendicular to the stretching maintained at zero. Periodic boundary conditions (PBC) were applied in all directions. The tensile tests were performed at 300 K, with strain rates set at $\dot{\epsilon} = 2 \times 10^8 1/s$ and $\dot{\epsilon} = 2 \times 10^9 1/s$.

To calculate the stacking fault energy, we obtained the generalized planar fault energy (GSFE) curves by incrementally displacing the top half of the simulation box by 0.01 Å along the (111) plane in the $[11\bar{2}]$ direction until a stacking fault formed. After each increment, the configuration underwent constrained energy minimization, allowing the system to relax only along the y direction. For visualization, we used OVITO software [59].

3. Results and discussion

3-1. Effect of Ti and Al in the formation of L_{12}

In this study, we employed hybrid MD/MC to investigate the formation of L_{12} NPs in four MPEAs: $(\text{CoNiFe})_{84}(\text{Al}_8\text{Ti}_8)$, $(\text{CoNiFe})_{86}(\text{Al}_7\text{Ti}_7)$, $(\text{CoNiFe})_{88}(\text{Al}_6\text{Ti}_6)$, and $(\text{CoNiFe})_{94}(\text{Al}_4\text{Ti}_2)$.

Fig. 1 presents these results. Fig. 1a shows the distribution of atoms after 14 million swaps at 300 K, where a Ni-rich L₁₂ phase formed in all four MPEAs. A Ni-rich L₁₂ phase was also observed in experimental studies for (CoNiFe)₈₆(Al₇Ti₇) MPEA [60]. Figs. 1b and 1d show the results at 300 K and 1000 K, respectively. (CoNiFe)₈₆(Al₇Ti₇) alloy contains the highest amount of L₁₂, while (CoNiFe)₉₄(Al₄Ti₂) alloy has the lowest. The L₁₂ atomic percentage decreases with increasing annealing temperature. The formation of the L₁₂ nanoprecipitate (NP) phase in these alloys is evidenced by the system reaching its lowest potential energy (see Figs. 1c and 1e). The spatial distribution of the L₁₂ phase across different alloy compositions is shown in Fig. S1.

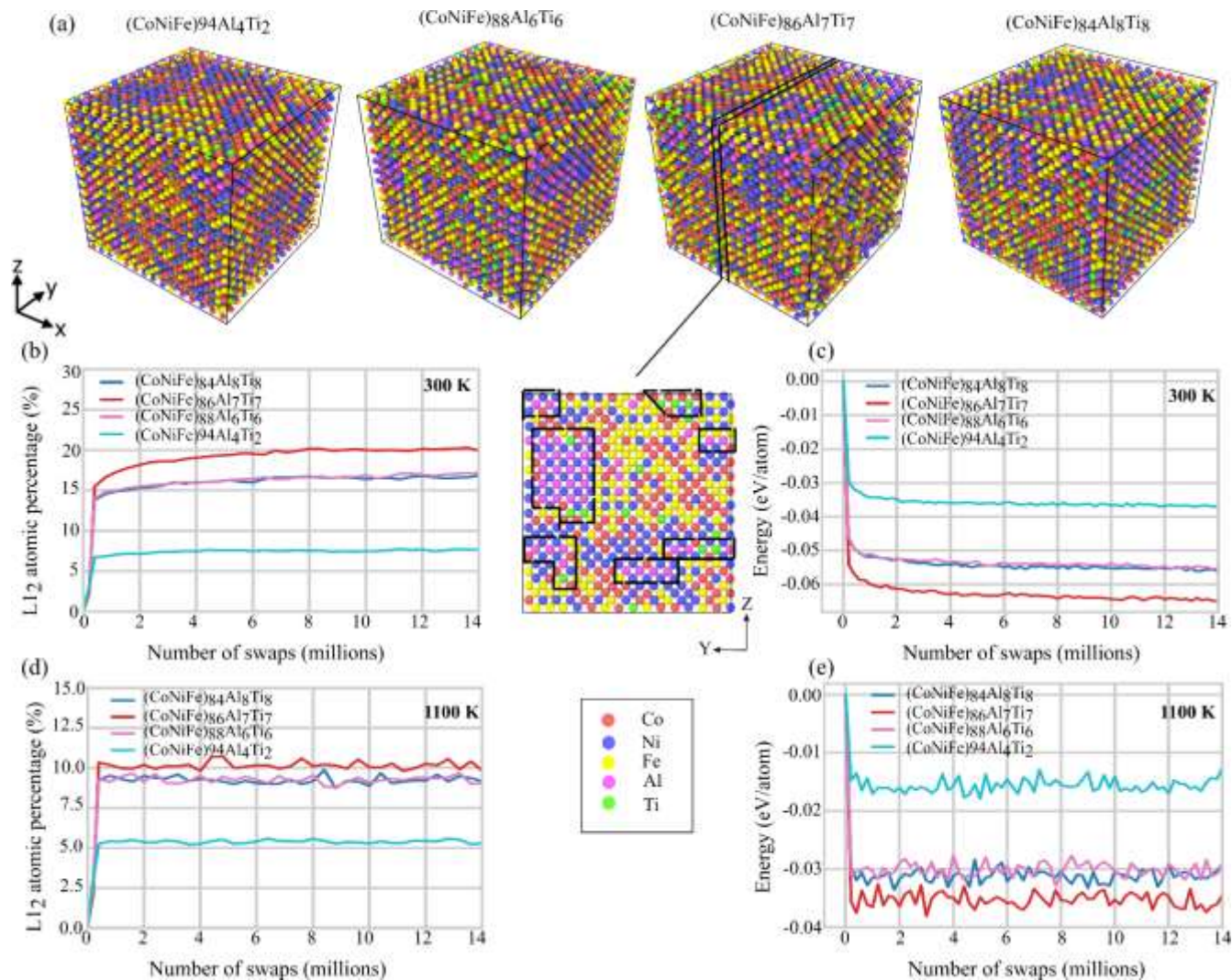


Fig. 1: Hybrid MD/MC simulation outcomes for four CoNiFeAlTi alloys, based on 14 million swap attempts: (a) Final atomic distribution at 300 K. (b-c) Variation in L₁₂ atomic percentage and associated potential energies with the number of swaps at 300 K. (d-e) Variation in L₁₂ atomic percentage and associated potential energies with the number of swaps at 1000 K

Although our simulations did not explicitly calculate the isolated formation energy of the L₁₂ phase itself, the significantly lower equilibrium potential energy observed at (CoNiFe)₈₆(Al₇Ti₇), compared to other compositions tested, strongly suggests that the formation of L₁₂ at this

composition is energetically favorable. Thus, the highest observed L_{12} fraction at $(\text{CoNiFe})_{86}(\text{Al}_7\text{Ti}_7)$ is indeed correlated with the alloy's enhanced energetic preference for ordering. Additionally, we have conducted a detailed analysis of the SRO using the Warren–Cowley parameters (WCP). The results reveal a strong ordering tendency among Ni–Al and Co–Ti atomic pairs in the first-nearest-neighbor shell. Among the investigated compositions, the $(\text{CoNiFe})_{86}(\text{Al}_7\text{Ti}_7)$ alloy exhibits the most pronounced Ni–Al ordering, while the $(\text{CoNiFe})_{94}(\text{Al}_4\text{Ti}_2)$ composition shows the weakest. These findings are consistent with the emergence of Ni-rich L_{12} -type local structures, in agreement with our calculations of the L_{12} phase. The computational details of the WCP analysis and a heatmap visualizing the results are included in the Supplementary Information (Fig. S2).

The variation in L_{12} phase volume fraction observed in our hybrid MD/MC simulations may reflect similar tendencies reported in earlier studies of CoNi-based MPEAs. For instance, studies on equimolar Co-Ni-based MPEAs with added Al and Ti report that the L_{12} volume fraction typically does not exceed 30% [60–62]. Additionally, adjustments in the Al/Ti ratio have been shown to influence phase distribution [62,63]. Specifically, Ding et al. demonstrated that a higher Al/Ti ratio could reduce the L_{12} phase volume fraction [62], which is consistent with our observation of a lower L_{12} fraction in $(\text{CoNiFe})_{94}(\text{Al}_4\text{Ti}_2)$ relative to $(\text{CoNiFe})_{86}(\text{Al}_7\text{Ti}_7)$. Another study indicates that increasing Ti content while keeping Al constant can raise the L_{12} phase volume fraction [63]. Although both Al and Ti contents change between $(\text{CoNiFe})_{86}(\text{Al}_7\text{Ti}_7)$ and $(\text{CoNiFe})_{88}(\text{Al}_6\text{Ti}_6)$ the relatively higher Ti content in the $(\text{CoNiFe})_{86}(\text{Al}_7\text{Ti}_7)$ alloy may partially contribute to its increased L_{12} phase fraction, in line with the trend reported in Ref. [63]. Furthermore, $(\text{CoNiFe})_{86}(\text{Al}_7\text{Ti}_7)$ has a higher L_{12} fraction than $(\text{CoNiFe})_{84}(\text{Al}_8\text{Ti}_8)$, which could be due to the effect of high Al concentrations in FCC HEAs. Excess Al in these alloys often promotes the formation of the B2 phase rather than the L_{12} phase [64]. These trends highlight that $(\text{CoNiFe})_{86}(\text{Al}_7\text{Ti}_7)$, with its balanced Al and Ti content, achieves the optimal conditions for a high L_{12} phase volume fraction, while alloys with higher Al or Al/Ti ratios (such as $(\text{CoNiFe})_{94}(\text{Al}_4\text{Ti}_2)$ and $(\text{CoNiFe})_{84}(\text{Al}_8\text{Ti}_8)$) show reduced L_{12} fractions, consistent with our findings.

3-2 Tensile properties

To study the effect of NPs on tensile properties, we conducted uniaxial tensile tests using MD on $(\text{CoNiFe})_{86}(\text{Al}_7\text{Ti}_7)$ and $(\text{CoNiFe})_{94}(\text{Al}_4\text{Ti}_2)$ alloys before and after hybrid MD/MC simulations. These two alloys were selected because they represent the highest and lowest L_{12} phase percentages among the four different alloys studied. For ease of identification, we refer to the ordered and random versions of $(\text{CoNiFe})_{84}(\text{Al}_8\text{Ti}_8)$, $(\text{CoNiFe})_{86}(\text{Al}_7\text{Ti}_7)$, $(\text{CoNiFe})_{88}(\text{Al}_6\text{Ti}_6)$, and $(\text{CoNiFe})_{94}(\text{Al}_4\text{Ti}_2)$ MPEAs as Al8Ti8-O and Al8Ti8-R, Al7Ti7-O and Al7Ti7-R, Al6Ti6-O and Al6Ti6-R, and Al4Ti2-O and Al4Ti2-R, respectively. To ensure robust statistics, we prepared 8 different samples (using different random seeds for initial distributions) for each alloy before and after hybrid MD/MC simulations. After hybrid MD/MC, we obtained 8 samples with nearly identical potential energies and L_{12} phase percentages but different local positions of L_{12} NPs.

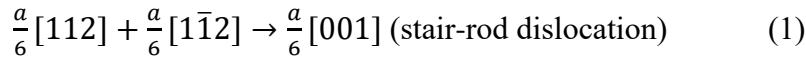
Tensile tests were performed at 300 K at two different strain rates: $\dot{\epsilon} = 2 \times 10^8 \text{1/s}$ and $\dot{\epsilon} = 2 \times 10^9 \text{1/s}$. Fig. 2a shows the direction of loading. Fig. 2 illustrates the results for Al7Ti7 at these two strain rates. Figs. 2b and 2c present the stress-strain curves for Al7Ti7-O and Al7Ti7-R (mean values for 8 samples) at 300 K under the two strain rates. Figs. 2d and 2e depict the evolution of dislocations during loading.

The strengthening mechanisms in Co-Ni-based MPEAs arise from NP strengthening and solid solution strengthening, both of which rely on dislocation interactions with precipitates or solute atoms. In tensile testing of single-crystal pristine samples without initial dislocations, the yield

point reflects a tendency for initial dislocation formation, while the flow stress represents the subsequent growth and interaction of these dislocations with NPs.

The stress-strain curves (Figs. 2b and 2c) demonstrate that the formation of an ordered phase containing $L1_2$ NPs increases yield strength and flow stress. At the lower strain rate ($\dot{\epsilon} = 2 \times 10^8 1/s$), the ordered phase (Al7Ti7-O) exhibits a neck, whereas the random distribution of atoms (Al7Ti7-R) shows a sudden drop in stress. This increase in yield strength and flow stress due to the formation of ordered phases in Co-Ni-based MPEAs has been previously reported [18,65].

To correlate this tensile behavior with dislocation dynamics, we analyzed the total dislocation length during tension (Figs. 2d and 2e). No clear, inferable difference was observed between the total dislocation lengths of Al7Ti7-O and Al7Ti7-R alloys during loading. Fig. 2 also shows that increasing strain rate results in higher yield strength and total dislocation length for both alloys. We further analyzed the amounts of Shockley dislocations and Stair-rod dislocations during tension (Fig. 3). This figure shows that the density of Stair-rod dislocations is significantly higher in Al7Ti7-O, whereas the density of Shockley dislocations is similar in both Al7Ti7-O and Al7Ti7-R. The formation of Stair-rod dislocations, which are sessile, can contribute to the increased strength in MPEAs [18,66–68]. The majority of dislocations formed in FCC alloys are glissile partial dislocations. Stair-rod dislocations typically form when partial dislocations on intersecting $\{111\}$ planes react as follows [69]:



$L1_2$ NPs may facilitate stair-rod dislocation formation by promoting the intersection of partial dislocations in their vicinity. This may be due to the high stacking fault energy (SFE) of the NPs (see Section 3.3), which, while locally suppressing the dissociation of partial dislocations, increases dislocation activity and intersection events in the surrounding matrix. This enhanced activity can, in turn, promote stair-rod formation. This explains the higher flow stress of the ordered Al7Ti7 alloy compared to the random alloy. Additionally, dislocation nodes developed by dislocation entanglement were also observed (Fig. 3c).

Fig. 4 compares the tensile properties of Al7Ti7-O and Al4Ti2-O alloys at two different strain rates. This figure further confirms the higher flow stress of Al7Ti7-O, which has a higher amount of $L1_2$ NPs. To understand the mechanical response differences between the Al4Ti2-O and Al7Ti7-O alloys, we compared their stress-strain curves before NP formation, using the Al4Ti2-R and Al7Ti7-R alloys with a random atomic distribution inside the crystal cell (see Fig. S4). In this random configuration, both the flow and yield stresses of the Al4Ti2-R alloy are higher than those of the Al7Ti7-R alloy. However, after NP formation, the Al7Ti7-O alloy exhibits a higher flow stress than Al4Ti2-O, even though Al4Ti2 maintains a higher yield stress (Fig. 4). To explain why Al4Ti2 alloys have a higher yield stress than Al7Ti7 alloys, we examined the tendency for dislocation formation by calculating the energy factors K , based on each alloy's elastic constants [70,71]:

$$K_{screw} = \left[\frac{C_{44}(C_{11} - C_{12})}{2} \right]^{\frac{1}{2}} \quad (2)$$

$$K_{edge} = (C_{11} + C_{12}) [C_{44}(C_{11} - C_{12}) / C_{11}(C_{11} + C_{12} + 2C_{44})]^{\frac{1}{2}} \quad (3)$$

For Al4Ti2-R alloy ($C_{11} = 253.38 \text{ GPa}$, $C_{12} = 161.53 \text{ GPa}$, $C_{44} = 97.74 \text{ GPa}$) we obtained $K_{screw} = 66.99 \text{ GPa}$ and $K_{edge} = 99.96 \text{ GPa}$. For Al7Ti7-R alloy ($C_{11} = 238.79 \text{ GPa}$, $C_{12} = 159.91 \text{ GPa}$, $C_{44} = 95.79 \text{ GPa}$) we obtained $K_{screw} = 61.46 \text{ GPa}$ and $K_{edge} = 92.31 \text{ GPa}$. A smaller K value signals that the alloy has a higher tendency for dislocation formation. These lower

energy factors for Al7Ti7-R alloy suggest a higher tendency for dislocation formation compared to Al4Ti2-R alloy, explaining the observed differences in yield stress between the alloys.

It should be noted that while the introduction of L1₂ NPs increases the yield strength of both Al7Ti7 and Al4Ti2 alloys, the magnitude of yield strength increase in Al7Ti7-O is not sufficient to overcome the baseline strength difference between the corresponding random alloys. In other words, although the yield strength of Al7Ti7-O benefits from L1₂ phase ordering, it remains lower than that of Al4Ti2-O due to its origin from a mechanically weaker matrix (Al7Ti7-R).

3-3 Stacking fault energy

Stacking fault energy is one of the important properties that play a key role in the mechanical behavior of FCC MPEAs [65,68,72–74]. The SFE was calculated by displacing the atomic plane by $a/6[112]$ (a is lattice constant) in the upper half of the simulation box. In $\gamma(FCC)/\gamma'(L1_2)$ alloys, this type of SFE is also referred to as complex SFE (CSFE) [57]. The first local minimum on the GSFE curve represents the most stable configuration and is identified as the SFE (Fig. 5b). To examine the dependency of SFE on the local environment, the Y coordinate of the moving plane was varied within the range of $[-20, 20]$ (see Fig. 5a). Figs. 5c-f display the stacking fault energy for the four alloys, both with random atomic distributions and with ordered L1₂ NPs. Table 1 provides the mean SFE values for each alloy.

As shown in Fig. 5 and Table 1, the presence of L1₂ NPs in these alloys leads to an increase in SFE. Previous studies have also reported an increase in SFE with the degree of SRO [39,65,75]. Furthermore, Table 1 reveals that increasing the aluminum and titanium content from Al4Ti2 to Al8Ti8 results in higher stacking fault energy. The rise in SFE with the addition of Al is well-documented in FCC systems [76,77].

Table 1: Mean value of SFE (mJ/m²) across various Y coordinates of the stacking fault plane for the four alloys, both with random atomic distributions and with ordered L1₂ NPs.

| | Al4Ti2 | Al6Ti6 | Al7Ti7 | Al8Ti8 |
|-------------------------|--------------|--------------|----------------|---------------|
| SFE before hybrid MD/MC | 19.54 ± 5.19 | 21.28 ± 7.13 | 25.53 ± 4.35 | 31.28 ± 8.01 |
| SFE after hybrid MD/MC | 86.07 ± 5.63 | 97.21 ± 9.11 | 111.58 ± 10.46 | 109.97 ± 6.97 |

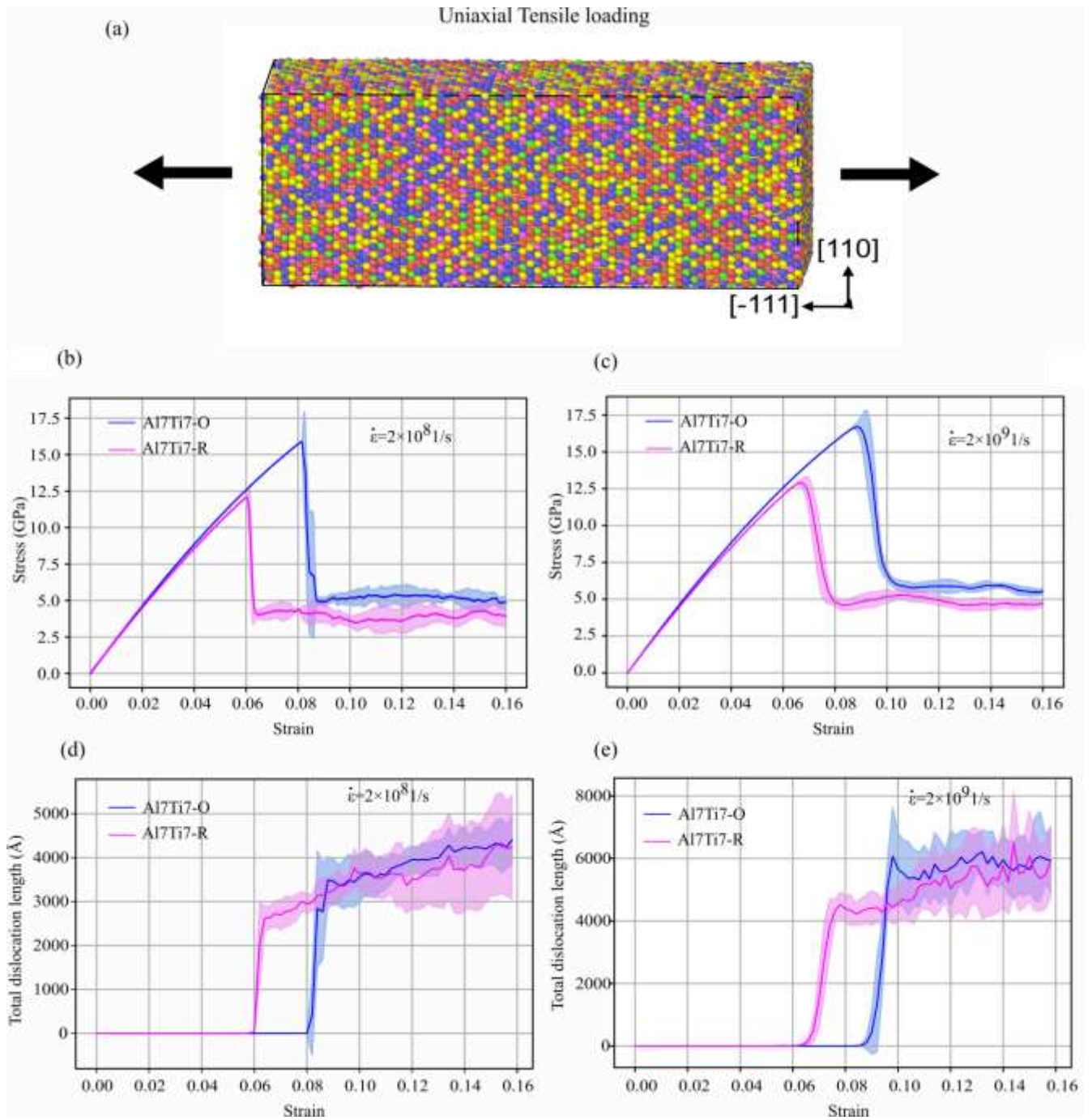


Fig. 2: Uniaxial tensile loading, stress-strain curves, and strain-dislocation length curves for $(\text{CoNiFe})_{86}(\text{Al}_7\text{Ti}_7)$ at 300K (a) Schematic of the simulation setup. (b-c) Stress-strain curves for Al7Ti7-O and Al7Ti7-R (mean values and standard deviations) under two strain rates. (d-e) Total dislocation length vs. strain for Al7Ti7-O and Al7Ti7-R (mean values and standard deviations) under two strain rates.

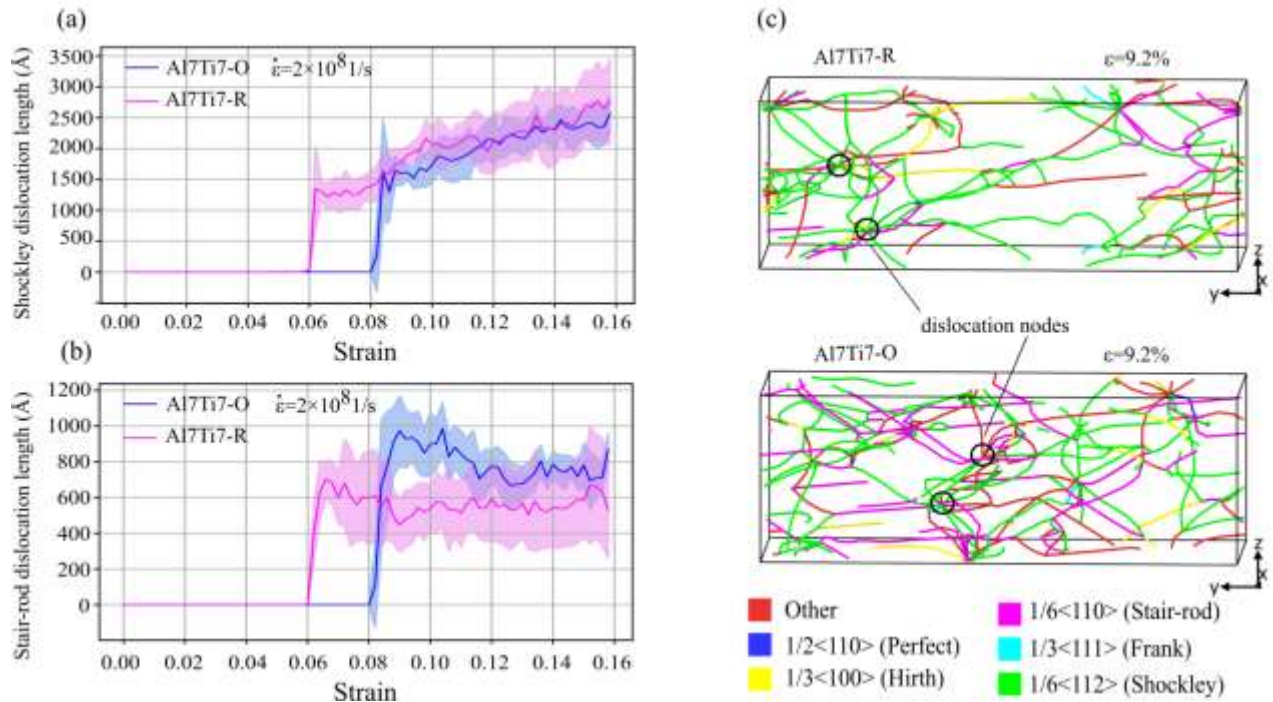


Fig. 3: (a-b) Comparison of Shockley dislocation lengths and Stair-rod dislocations during loading for Al7Ti7-O and Al7Ti7-R alloys (c) Visualization of dislocations at $\epsilon = 9.2\%$ for Al7Ti7-O and Al7Ti7-R alloys.

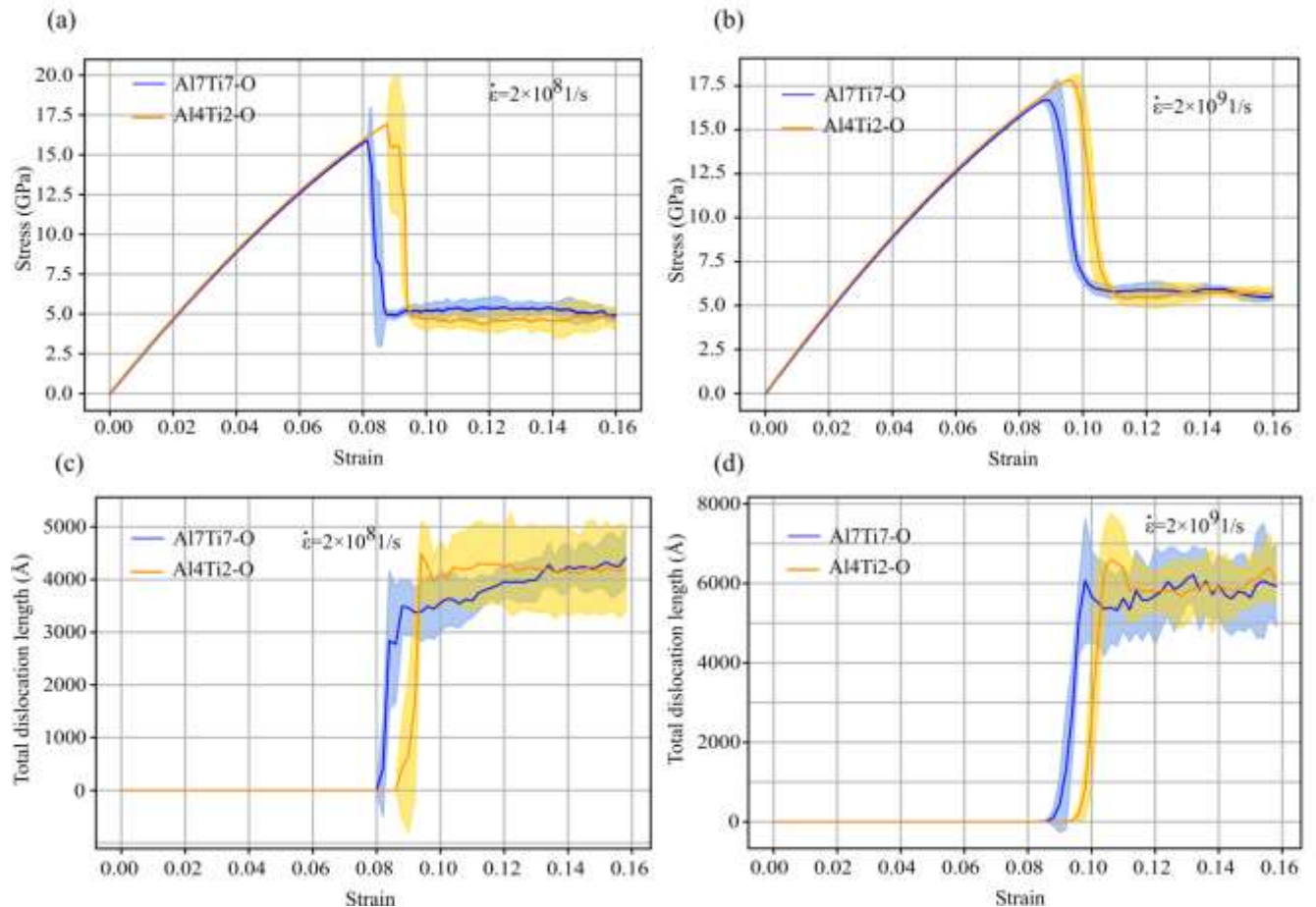


Fig. 4: (a-b) Stress-strain curves for Al₇Ti₇-O and Al₄Ti₂-O (mean values and standard deviations) under two tensile strain rates at 300 K. (d-e) Total dislocation length vs. strain for Al₇Ti₇-O and Al₄Ti₂-O (mean values and standard deviations) under two strain rates.

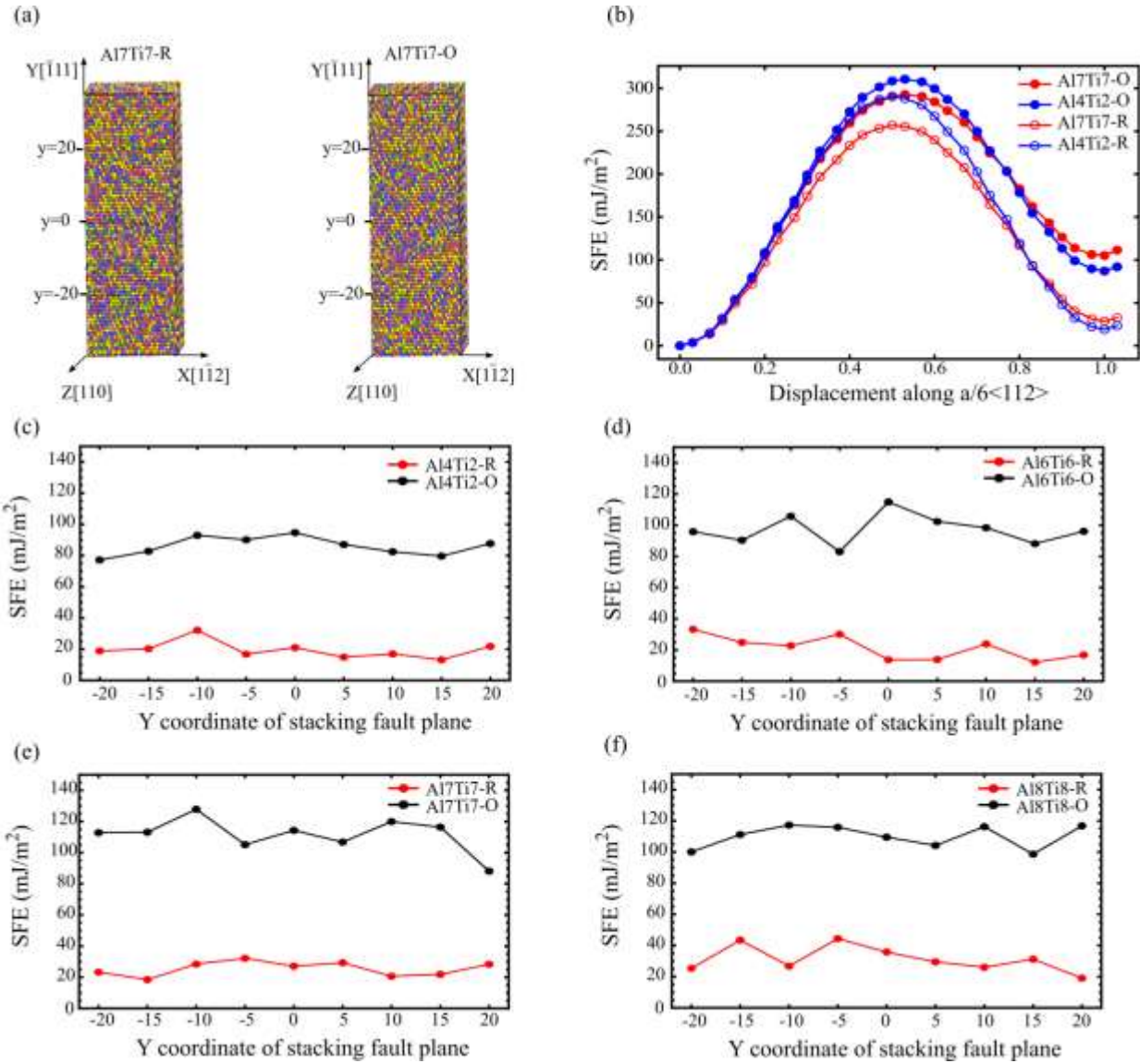


Fig. 5: (a) Schematic of the simulation box showing the Y coordinate of the moving plane within the range of $[-20, 20]$ to examine the dependency of stacking fault energy (SFE) on the local environment. (b) GSFE curves for Al₇Ti₇-O and Al₇Ti₇-R, Al₄Ti₂-O, and Al₄Ti₂-R alloys for a representative Y value within the specified range. (c-f) Stacking fault energy for the four alloys, both with random atomic distributions and with ordered L₂ NPs.

3-4 Dislocation-nanoprecipitate interaction

To investigate how L₂ NPs affect dislocation pinning, an edge dislocation was introduced into the simulation box for the (CoNiFe)₈₆Al₇Ti₇ alloy. This composition was chosen because it contains the highest amount of L₂. After relaxation, this edge dislocation dissociated into two partial dislocations, referred to as the trailing and leading partial dislocations. NPs with diameters of 4, 6,

and 8 nm were positioned relative to the dislocation (see Fig. 6). The composition of the matrix and L1₂ NPs was extracted from Ref. [60], where the L1₂ NP has a (Ni,Co,Fe)₃(Ti,Al,Fe) structure. In our model, a spherical L1₂ NP was embedded within a chemically random FCC matrix. A pure Ni crystal was first constructed and oriented along $X = [1\bar{1}0]$, $Y = [11\bar{2}]$ and $Z = [111]$ directions. A spherical region was then carved out and replaced with an L1₂-structured Ni₃Al-type domain of the same diameter and lattice constant to ensure coherency. Within this sphere, 32% of Ni atoms were substituted with Co, 12% with Fe, and the remainder kept as Ni (56%). Within this sphere, 32% of Ni atoms were substituted with Co, 12% with Fe, and 56% remained as Ni. On the Al sublattice, 54% of Al atoms were replaced by Ti, 11% by Fe, and 35% remained as Al. The overall elemental composition of the L1₂ NP was 42% Ni, 24% Co, 11.7% Fe, 8.8% Al, and 13.5% Ti, which is close to the L1₂ composition reported in Ref. [60]. Outside the NP, Co, Fe, Al, and Ti were randomly substituted into the Ni matrix to achieve the target alloy composition of (CoNiFe)₈₆(Al₇Ti₇). Due to the low lattice misfit between the ordered L1₂ phase and the surrounding matrix, the interface was coherent and crystallographically aligned.

The simulation box has dimensions of 511.1 Å × 100.3 Å × 620.8 Å, oriented with $X = [1\bar{1}0]$, $Y = [11\bar{2}]$ and $Z = [111]$. To study the interaction between NPs and dislocations, shear strain-controlled loading at a rate of $8 \times 10^6 \text{ s}^{-1}$ was applied. Periodic boundary conditions were used in X and Y directions, with a fixed boundary condition in the Z direction. The Z-directional volume was divided into three regions: a central area containing typical MD mobile atoms, positioned between fixed upper and lower regions. The fixed upper and lower regions consist of several atomic layers (grey layers in Fig. 6). After relaxation, a constant strain rate was implemented through shear strain loading, achieved by applying velocity along the positive x direction to the upper region while keeping the lower region fixed. During this loading process, the microcanonical ensemble (NVE) was used in conjunction with Langevin dynamics in the central region. To minimize the potential impact of local thermal activation on dislocation behavior, Langevin dynamics maintained the system temperature at approximately 5 K.

The results are shown in Fig. 7. The results are compared with equimolar CoNiFe without any ordered phase. This figure show that increasing NP size from 4 to 8 nm in (CoNiFe)₈₆Al₇Ti₇ alloy led to an increase in depinning stress at 5 K, rising from 340 MPa to 450 MPa. No Orowan-looping was observed after the dislocation passed through the L1₂ NPs in this alloy. The only mechanism observed was dislocation cutting within this NP size range (Fig. 8). We calculated the atomic mismatch percentage between the L1₂ NPs and the FCC matrix using the following formula: $\delta = \frac{2(a_{L1_2} - a_{FCC})}{a_{L1_2} + a_{FCC}} \times 100$, where a_{FCC} represents the lattice constant for the random composition and a_{L1_2} represents the lattice constant for the site with the L1₂ structure. To calculate the lattice constant, we analyzed the first peak of the radial distribution function $g(r)$ for both systems: a random FCC with (CoNiFe)₈₆Al₇Ti₇ composition and a system with the corresponding L1₂ composition after minimization at 0 K (Fig. S3). By considering the pair separation distance at the first peak as the first nearest neighbor atom distance ($a/\sqrt{2}$) in these compositions, we calculated $a_{FCC} = 3.596 \text{ \AA}$ and $a_{L1_2} = 3.601 \text{ \AA}$. This results in $\delta = 0.139\%$ which is very close to the experimental lattice mismatch for (CoNiFe)₈₆Al₇Ti₇ MPEA(0.21%) [60]. The small positive lattice mismatch indicates the formation of coherent NPs in (CoNiFe)₈₆Al₇Ti₇. This small lattice mismatch alone should not be the primary reason for the increase in depinning stress by approximately 110 MPa when the size of the NPs increases from 4 to 8 nm. Therefore, we sought a more substantial physical explanation. Figs. 7b-h provide an interesting clue, showing that the distance between the two partial dislocations inside and outside the NP differs. Given that this distance is inversely proportional to the stacking fault energy [75], it suggests that the SFE in the L1₂ NP is higher than in the matrix. Increases in SFE and decreases in dislocation distance with increasing SRO have

been reported in experimental results for VCoNi [75]. We calculated the stacking fault energy for a system with the same composition as the L1₂ NPs using the same method described in the previous section. Additionally, we calculated the stacking fault energy mismatch as follows: $\delta_{SFE} = \frac{2(SFE_{L1_2} - SFE_{FCC})}{SFE_{L1_2} + SFE_{FCC}}$. We calculated $SFE_{L1_2} = 337.36 \pm 13.95 \text{ mJ/m}^2$, which is consistent with DFT values reported for the (Ni,Co,Fe)₃(Ti,Al,Fe) L1₂ structure (354 mJ/m^2) [57]. By extracting SFE_{FCC} from Table 1 for the random distribution of (CoNiFe)₈₆Al₇Ti₇ alloy ($25.53 \pm 4.3 \text{ mJ/m}^2$), we calculated $\delta_{SFE} = 1.178$, representing a large SFE mismatch (117.8%) between the precipitate and the matrix. The difference in stacking fault energy between the matrix and NPs induces a pinning force as dislocations pass through, despite the small lattice mismatch between the NPs and the matrix. This results are supported by other studies, which have shown that the strength of alloys can be increased by larger fluctuations in the stacking fault energy [78,79]. These results suggest that a low lattice mismatch combined with a high stacking fault energy mismatch between the NPs and the matrix can be an effective strategy for increasing strength without sacrificing ductility. We did not observe any Orowan loops after dislocations passed through L1₂ precipitates with sizes up to 8 nm. The relative size of the dislocation line and NPs may influence the depinning stress and potentially alter the interaction mechanism [80,81]. To ensure that the dislocation line length does not affect the observed mechanism, we performed additional simulations with a longer dislocation line ($Y \approx 32 \text{ nm}$) interacting with an 8 nm L1₂ NP. No evidence of Orowan looping was observed, even after multiple dislocation-NP interactions. Fig. 8 shows the cutting of precipitates after multiple dislocation passes. The low lattice misfit may be responsible for the absence of Orowan loops.

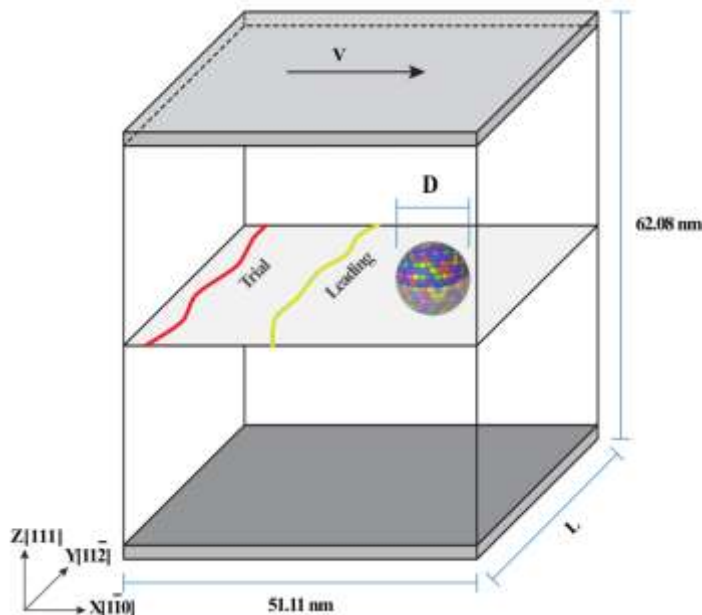


Fig. 6: Schematic of the simulation box used for performing shear strain control loading to study dislocation-nanoprecipitate interaction in (CoNiFe)₈₆Al₇Ti₇ alloy.

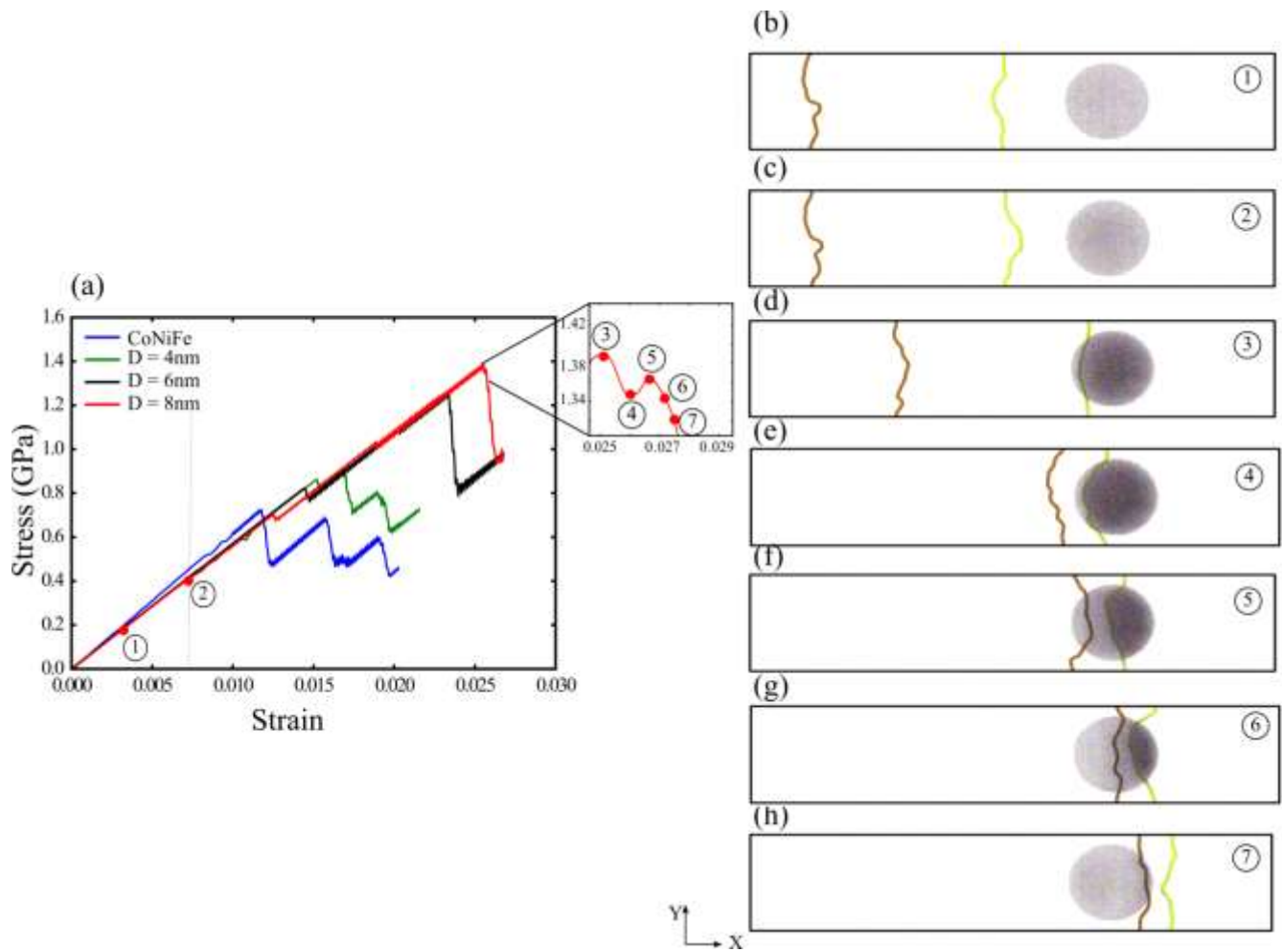


Fig. 7: (a) Stress–strain curves under shear loading for $(\text{CoNiFe})_{86}\text{Al}_7\text{Ti}_7$ containing an edge dislocation and a spherical nanoprecipitate (NP) of varying diameters. For comparison, the shear response of equimolar CoNiFe with an edge dislocation but without NPs is also shown. (b–h) Snapshots of the simulation box illustrating the dislocation and an 8 nm NP at points 1–7 indicated on the stress–strain curve.

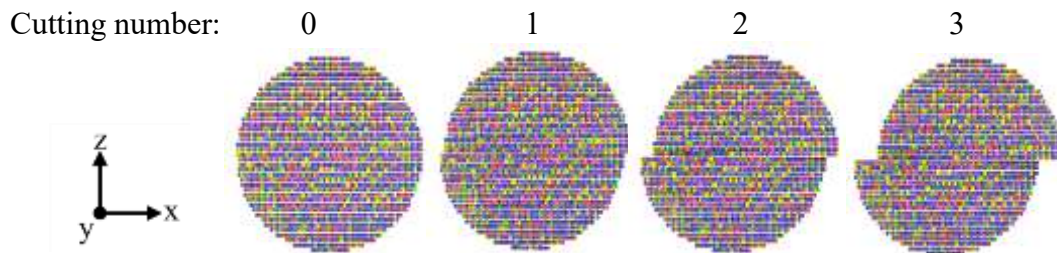


Fig. 8: Snapshot of a nanoprecipitate with a diameter of 8 nm after several passes of a dislocation (cutting numbers) through it

4. Conclusions

In this study, we explored the effects of Ti and Al concentrations on the formation of L1₂ nanoprecipitates and their influence on the mechanical properties of CoNiFeAlTi MPEAs using atomistic simulations. Our key findings are:

- 1- L1₂ nanoprecipitate formation: Using hybrid MD/MC simulations at 300 K and 1100 K, we observed the formation of Ni-rich L1₂ NPs in four MPEAs: (CoNiFe)₈₄(Al₈Ti₈), (CoNiFe)₈₆(Al₇Ti₇), (CoNiFe)₈₈(Al₆Ti₆), and (CoNiFe)₉₄(Al₄Ti₂) MPEAs. Among these, the (CoNiFe)₈₆(Al₇Ti₇) alloy demonstrated the highest concentration of L1₂ NPs, highlighting its potential for achieving a balanced combination of strength and ductility.
- 2- Enhanced tensile properties: The presence of L1₂ NPs significantly increased the yield strength and flow stress of the alloys. Specifically, the ordered phases containing L1₂ NPs in the (CoNiFe)₈₆(Al₇Ti₇) alloy exhibited higher yield strength and flow stress compared to their random counterparts. The formation of more sessile Stair-rod dislocations in the alloy containing L1₂ may be responsible for the increased flow stress.
- 3- Dislocation-Nanoprecipitate interactions: Our analysis revealed that dislocations primarily shear through L1₂ NPs rather than bypass them via the Orowan mechanism. This dislocation-cutting mechanism, observed in NPs sized 4-8 nm, contributed significantly to the material's strengthening.
- 4- Stacking Fault Energy (SFE): Hybrid MD/MC results indicate that the formation of L1₂ NPs correlates with an overall increase in the calculated SFE of the alloy system. The substantial difference in SFE between the NPs and the FCC matrix enhanced dislocation pinning, leading to increased material strength.

In summary, our findings highlight the variation in the amount of L1₂ phase achieved by adjusting Al and Ti concentrations, identifying the optimal values for maximizing L1₂ phase formation. This study demonstrates a novel strategy for designing MPEAs with enhanced strength and ductility by leveraging low lattice mismatch and high stacking fault energy mismatch between precipitates and the matrix. The insights gained from this research lay a solid foundation for designing new MPEAs with tailored properties, effectively balancing strength and ductility through nanoscale precipitation engineering. This work not only advances the understanding of nanoprecipitate behavior in complex alloys but also provides practical guidance for future material design and optimization efforts

Acknowledgments

This research was funded by the European Union Horizon 2020 research and innovation program under NOMATEN Teaming grant (agreement no. 857470) and from the European Regional Development Fund via the Foundation for Polish Science International Research Agenda PLUS program grant No.MAB PLUS/2018/8. The publication was created within the framework of the project of the Minister of Science and Higher Education "Support for the activities of Centres of Excellence established in Poland under Horizon 2020" under contract no. MEiN/2023/DIR/3795.

We acknowledge the computational resources provided by the High Performance Cluster at the National Centre for Nuclear Research in Poland.

Data availability

Data will be made available on request.

References

- [1] B. Gludovatz, A. Hohenwarter, D. Catoor, E.H. Chang, E.P. George, R.O. Ritchie, A fracture-resistant high-entropy alloy for cryogenic applications, *Science* (80-.). 345 (2014) 1153–1158. <https://doi.org/10.1126/SCIENCE.1254581>
- [2] Y.F. Ye, Q. Wang, J. Lu, C.T. Liu, Y. Yang, High-entropy alloy: challenges and prospects, *Mater. Today*. 19 (2016) 349–362. <https://doi.org/10.1016/J.MATTOD.2015.11.026>.
- [3] M. Slobodyan, E. Pesterev, A. Markov, Recent advances and outstanding challenges for implementation of high entropy alloys as structural materials, *Mater. Today Commun.* 36 (2023) 106422. <https://doi.org/10.1016/J.MTCOMM.2023.106422>.
- [4] J.M. Park, D.C. Yang, H.J. Kim, D.G. Kim, S. Lee, H.S. Kim, S.S. Sohn, Ultra-strong and strain-hardenable ultrafine-grained medium-entropy alloy via enhanced grain-boundary strengthening, *Mater. Res. Lett.* 9 (2021) 315–321. <https://doi.org/10.1080/21663831.2021.1913768>.
- [5] O.N. Senkov, G.B. Wilks, J.M. Scott, D.B. Miracle, Mechanical properties of Nb₂₅Mo₂₅Ta₂₅W₂₅ and V₂₀Nb₂₀Mo₂₀Ta₂₀W₂₀ refractory high entropy alloys, *Intermetallics*. 19 (2011) 698–706. <https://doi.org/10.1016/J.INTERMET.2011.01.004>.
- [6] Y.K. Kim, S. Yang, K.A. Lee, Superior Temperature-Dependent Mechanical Properties and Deformation Behavior of Equiatomic CoCrFeMnNi High-Entropy Alloy Additively Manufactured by Selective Laser Melting, *Sci. Reports* 2020 101. 10 (2020) 1–13. <https://doi.org/10.1038/s41598-020-65073-2>.
- [7] Z. Luo, Q. Liu, J. Wei, X. Huang, Z. Gao, Z. Wang, X. Ma, Enhancing the strength-ductility synergy of dual-phase Al_{0.3}CoCrFeNiTi_{0.3} high-entropy alloys through the regulation of B2 phase content, *Mater. Sci. Eng. A*. 916 (2024) 147346. <https://doi.org/10.1016/J.MSEA.2024.147346>.
- [8] H. Liu, T. Li, C. Chen, M. Wan, C. Huang, J. Li, Unraveling the fracture behavior of AlCoCrFeNi_{2.1} eutectic high-entropy alloy under impact loading, *J. Mater. Sci. Technol.* 214 (2025) 170–179. <https://doi.org/10.1016/J.JMST.2024.06.040>.
- [9] Q. Zhang, Z. Chen, Y. Dong, C. Li, Y. Wang, High strength and ductility eutectic high entropy alloy with unique core-shell structure, *J. Alloys Compd.* 976 (2024) 173141. <https://doi.org/10.1016/J.JALLCOM.2023.173141>.
- [10] G. Talluri, M. Nagini, D.A. Babu, Y. Palguna, K. Rajesh, B.S. Murty, R.S. Maurya, Designing a eutectic multi-principal element alloy for strength-ductility synergy, *J. Alloys Compd.* 976 (2024) 173278. <https://doi.org/10.1016/J.JALLCOM.2023.173278>.
- [11] *Advanced Materials - 2018 - Sohn - Ultrastrong Medium-Entropy Single-Phase Alloys Designed via Severe Lattice Distortion.pdf*, (n.d.).
- [12] A. Esfandiarpour, S. Papanikolaou, M. Alava, Edge dislocations in multicomponent solid solution alloys: Beyond traditional elastic depinning, *Phys. Rev. Res.* 4 (2022). <https://doi.org/10.1103/PhysRevResearch.4.L022043>.
- [13] A. Esfandiarpour, R. Alvarez-Donado, S. Papanikolaou, M. Alava, Atomistic simulations of dislocation plasticity in concentrated VCoNi medium entropy alloys: Effects of lattice distortion and short range order, *Front. Mater.* 9 (2022) 1–11. <https://doi.org/10.3389/fmats.2022.1046291>.
- [14] K.Y. Xie, D. Yadav, B.L. Hackett, Y. Zhang, R. Patel, Y.C. Lai, G. Turner, I. Karaman, G.M.

- Pharr, Weak strain-rate sensitivity of hardness in the VCoNi equi-atomic medium entropy alloy, *Mater. Sci. Eng. A.* 913 (2024) 147091. <https://doi.org/10.1016/J.MSEA.2024.147091>.
- [15] D. Hua, Q. Zhou, Y. Shi, S. Li, K. Hua, H. Wang, S. Li, W. Liu, Revealing the deformation mechanisms of $\langle 110 \rangle$ symmetric tilt grain boundaries in CoCrNi medium-entropy alloy, *Int. J. Plast.* 171 (2023) 103832. <https://doi.org/10.1016/J.IJPLAS.2023.103832>.
- [16] D. Hua, Q. Xia, W. Wang, Q. Zhou, S. Li, D. Qian, J. Shi, H. Wang, Atomistic insights into the deformation mechanism of a CoCrNi medium entropy alloy under nanoindentation, *Int. J. Plast.* 142 (2021) 102997. <https://doi.org/10.1016/J.IJPLAS.2021.102997>.
- [17] A.H. Naghdi, K. Karimi, A.E. Poisvert, A. Esfandiarpour, R. Alvarez, P. Sobkowicz, M. Alava, S. Papanikolaou, Dislocation plasticity in equiatomic NiCoCr alloys: Effect of short-range order, *Phys. Rev. B.* 107 (2023) 1–13. <https://doi.org/10.1103/PhysRevB.107.094109>.
- [18] A. Jarlöv, W. Ji, R. Babicheva, Y. Tian, Z. Hu, H.L. Seet, L. Tan, F. Liu, Y. Liu, M.L.S. Nai, U. Ramamurty, K. Zhou, Tailoring short-range order and dislocation evolution in Cr–Co–Ni medium-entropy alloys: A molecular dynamics study, *Mater. Des.* 240 (2024) 112840. <https://doi.org/10.1016/J.MATDES.2024.112840>.
- [19] K. Hagihara, Effect of short-range order on the high-temperature plastic deformation behavior of Ni–Cr–W, Ni–W, and Ni–Re single crystals, *J. Mater. Sci. Technol.* 165 (2023) 143–152. <https://doi.org/10.1016/J.JMST.2023.04.058>.
- [20] L. Xu, Y. Ma, Z. Zhang, M. Yang, P. Jiang, Y. Zhu, X. Wu, F. Yuan, Superior tensile properties induced by triple-level heterogeneous structures in the CoNiV-based medium-entropy alloy, *J. Mater. Sci. Technol.* 214 (2025) 245–254. <https://doi.org/10.1016/J.JMST.2024.07.020>.
- [21] Y. Liu, H. Zhang, Y. Yang, L. Sun, X. Zhao, H. Le Yan, Y. Shen, N. Jia, Chemical short-range order dependence of micromechanical behavior in CoCrNi medium-entropy alloy studied by atomic simulations, *J. Alloys Compd.* 968 (2023) 172002. <https://doi.org/10.1016/J.JALLCOM.2023.172002>.
- [22] L. Han, F. Maccari, I.R. Souza Filho, N.J. Peter, Y. Wei, B. Gault, O. Gutfleisch, Z. Li, D. Raabe, A mechanically strong and ductile soft magnet with extremely low coercivity, *Nat.* 2022 6087922. 608 (2022) 310–316. <https://doi.org/10.1038/s41586-022-04935-3>.
- [23] Y. Liu, T. Ye, Q. Zhou, Y. Wu, S. Duan, T. Fan, Z. Wang, P. Tang, High-throughput prediction of intrinsic properties of L12-(Ni_x1,Cr_x2,Cox3)₃(Al_y1,Ti_y2) precipitates, *Mater. Today Commun.* 31 (2022) 103655. <https://doi.org/10.1016/J.MTCOMM.2022.103655>.
- [24] W. Mao, L. Yang, F. Jiang, J. He, J. Luan, Z. Jiao, F. Ren, Achieving ultrahigh strength in oxide-dispersion-strengthened CoCrNi alloy via in situ formation of coherent Y-Ti-O nanoprecipitates, *Mater. Des.* 232 (2023) 112141. <https://doi.org/10.1016/J.MATDES.2023.112141>.
- [25] Y.L. Zhao, Y.R. Li, G.M. Yeli, J.H. Luan, S.F. Liu, W.T. Lin, D. Chen, X.J. Liu, J.J. Kai, C.T. Liu, T. Yang, Anomalous precipitate-size-dependent ductility in multicomponent high-entropy alloys with dense nanoscale precipitates, *Acta Mater.* 223 (2022). <https://doi.org/10.1016/j.actamat.2021.117480>.
- [26] J.M. Guo, B.C. Zhou, S. Qiu, H.J. Kong, M.C. Niu, J.H. Luan, T.L. Zhang, H. Wu, Z.B. Jiao, Achieving ultrahigh strength and ductility in high-entropy alloys via dual precipitation, *J. Mater. Sci. Technol.* 166 (2023) 67–77. <https://doi.org/10.1016/J.JMST.2023.05.021>.
- [27] K. Huang, Y. Zhang, Z. Zhang, Y. Yu, J. Li, J. Han, K. Dong, P.K. Liaw, I. Baker, L. Sun, Coupling precipitation strengthening and transformation induced plasticity to produce a superior combination of strength and ductility in a high entropy alloy, *J. Alloys Compd.* 929 (2022) 167356. <https://doi.org/10.1016/J.JALLCOM.2022.167356>.
- [28] W. Zhang, R. Tang, Z.B. Yang, C.H. Liu, H. Chang, J.J. Yang, J.L. Liao, Y.Y. Yang, N. Liu, Preparation, structure, and properties of high-entropy alloy multilayer coatings for nuclear fuel cladding: A case study of AlCrMoNbZr/(AlCrMoNbZr)N, *J. Nucl. Mater.* 512 (2018) 15–24. <https://doi.org/10.1016/J.JNUCMAT.2018.10.001>.

- [29] P. Pandey, M. Heczko, N. Khatavkar, N. Mazumder, A. Sharma, A. Singh, M.J. Mills, K. Chattopadhyay, On the faulting and twinning mediated strengthening and plasticity in a γ' strengthened CoNi-based superalloy at room temperature, *Acta Mater.* 252 (2023) 118928. <https://doi.org/10.1016/j.actamat.2023.118928>.
- [30] L. Gao, Y. Wu, N. An, J. Chen, X. Liu, R. Bai, X. Hui, Nanoscale L12 phase precipitation induced superb ambient and high temperature mechanical properties in Ni–Co–Cr–Al system high-entropy superalloys, *Mater. Sci. Eng. A.* 898 (2024) 145995. <https://doi.org/10.1016/J.MSEA.2023.145995>.
- [31] L. Wang, L. Kong, Y. Li, Y. Wu, H. Su, Y. Su, B. Deng, G. Liu, Z. Han, Y. Zhang, J. Shen, G. Zhang, A novel (CoFeNi)₈₂Ti₅Al₅V₈ medium entropy alloy showing an ultra yield strength and a good ductility by L12 nanoparticles strengthening and dislocation strengthening, *Mater. Sci. Eng. A.* 893 (2024) 146138. <https://doi.org/10.1016/J.MSEA.2024.146138>.
- [32] L. Wang, X. Wu, Y. Wu, G. Liu, Z. Han, Y. Zhang, Y. Su, S. Kang, J. Shen, G. Zhang, Design and high-strength origin of novel (CoFeNi)₈₀Ti₅V₁₅ medium entropy alloy with “fcc + L12” structure, *J. Mater. Sci. Technol.* 149 (2023) 154–160. <https://doi.org/10.1016/J.JMST.2023.01.002>.
- [33] K. Tu, B. Li, Z. Li, K. Ming, S. Zheng, Dual heterogeneous structure enabled ultrahigh strength and ductility across a broad temperature range in CrCoNi-based medium-entropy alloy, *J. Mater. Sci. Technol.* 207 (2025) 46–59. <https://doi.org/10.1016/J.JMST.2024.01.091>.
- [34] J. Huang, W. Li, T. Yang, T.H. Chou, R. Zhou, B. Liu, J.C. Huang, Y. Liu, An additively manufactured precipitation hardening medium entropy alloy with excellent strength-ductility synergy over a wide temperature range, *J. Mater. Sci. Technol.* 197 (2024) 247–264. <https://doi.org/10.1016/J.JMST.2024.02.077>.
- [35] Y. Yang, J. Pang, Z. Zhang, Y. Wang, Y. Ji, Z. Zhu, L. Zhang, A. Wang, H. Zhang, H. Zhang, Strength-ductility synergy and superior strain-hardening ability of Ni₃₈Co₂₅Fe₁₃Cr₁₀Al₇Ti₇ multi principal element alloy through heterogeneous L12 structure modulation, *J. Alloys Compd.* 984 (2024) 173916. <https://doi.org/10.1016/J.JALLCOM.2024.173916>.
- [36] Z. Tai, X. Wang, X. Zong, X. Ding, J. Liu, F. Kong, Microstructure and mechanical properties of an elevated temperature L12-type Ni-Co-Cr-Al-Ti-V-B-based high-entropy intermetallic, *J. Alloys Compd.* 1010 (2025) 177262. <https://doi.org/10.1016/J.JALLCOM.2024.177262>.
- [37] X. Zhu, Y. He, Q. Feng, N. Wang, C. Ge, Y. Xu, Deformation mechanism of L12-type multicomponent intermetallics: The generalized stacking fault energy and chemical bonds, *Mater. Des.* 228 (2023) 111824. <https://doi.org/10.1016/J.MATDES.2023.111824>.
- [38] X. Huang, L. Liu, X. Duan, W. Liao, J. Huang, H. Sun, C. Yu, Atomistic simulation of chemical short-range order in HfNbTaZr high entropy alloy based on a newly-developed interatomic potential, *Mater. Des.* 202 (2021) 109560. <https://doi.org/10.1016/J.MATDES.2021.109560>.
- [39] Q.J. Li, H. Sheng, E. Ma, Strengthening in multi-principal element alloys with local-chemical-order roughened dislocation pathways, *Nat. Commun.* 2019 101. 10 (2019) 1–11. <https://doi.org/10.1038/s41467-019-11464-7>.
- [40] A.F. Andreoli, A. Fantin, S. Kasatikov, V.P. Bacurau, M. Widom, P. Gargarella, E.M. Mazzer, T.G. Woodcock, K. Nielsch, F.G. Coury, The impact of chemical short-range order on the thermophysical properties of medium- and high-entropy alloys, *Mater. Des.* 238 (2024) 112724. <https://doi.org/10.1016/J.MATDES.2024.112724>.
- [41] E. Wyszowska, C. Mieszczynski, Kurpaska, A. Azarov, W. Chromiński, I. Jóźwik, A. Esfandiarpour, A. Kosińska, D. Kalita, R. Diduszko, J. Jagielski, S.T. Nori, M. Alava, The Fe addition as an effective treatment for improving the radiation resistance of fcc Ni_xFe_{1-x} single-crystal alloys, *J. Nucl. Mater.* 584 (2023) 154565. <https://doi.org/10.1016/J.JNUCMAT.2023.154565>.
- [42] L. Zhou, Q. Wang, J. Wang, X. Chen, P. Jiang, H. Zhou, F. Yuan, X. Wu, Z. Cheng, E. Ma,

- Atomic-scale evidence of chemical short-range order in CrCoNi medium-entropy alloy, *Acta Mater.* 224 (2022) 117490. <https://doi.org/10.1016/J.ACTAMAT.2021.117490>.
- [43] A. Stukowski, V. V. Bulatov, A. Arsenlis, Automated identification and indexing of dislocations in crystal interfaces, *Model. Simul. Mater. Sci. Eng.* 20 (2012) 085007. <https://doi.org/10.1088/0965-0393/20/8/085007>.
- [44] A.P. Thompson, H.M. Aktulga, R. Berger, D.S. Bolintineanu, W.M. Brown, P.S. Crozier, P.J. in 't Veld, A. Kohlmeyer, S.G. Moore, T.D. Nguyen, R. Shan, M.J. Stevens, J. Tranchida, C. Trott, S.J. Plimpton, LAMMPS - a flexible simulation tool for particle-based materials modeling at the atomic, meso, and continuum scales, *Comput. Phys. Commun.* 271 (2022) 108171. <https://doi.org/10.1016/J.CPC.2021.108171>.
- [45] J.S. Kim, D. Seol, B.J. Lee, Critical assessment of Pt surface energy – An atomistic study, *Surf. Sci.* 670 (2018) 8–12. <https://doi.org/10.1016/J.SUSC.2017.12.008>.
- [46] M.I. Baskes, B.J. Lee, H. Kim, Y. Koo Cho, Second nearest-neighbor modified embedded atom method potentials for bcc transition metals, *Phys. Rev. B.* 64 (2001) 184102. <https://doi.org/10.1103/PhysRevB.64.184102>.
- [47] B.J. Lee, J.H. Shim, I. Baskes, Semiempirical atomic potentials for the fcc metals Cu, Ag, Au, Ni, Pd, Pt, Al, and Pb based on first and second nearest-neighbor modified embedded atom method, *Phys. Rev. B.* 68 (2003) 144112. <https://doi.org/10.1103/PhysRevB.68.144112>.
- [48] Y.M. Kim, B.J. Lee, M.I. Baskes, Modified embedded-atom method interatomic potentials for Ti and Zr, *Phys. Rev. B - Condens. Matter Mater. Phys.* 74 (2006) 014101. <https://doi.org/10.1103/PHYSREVB.74.014101>.
- [49] W.M. Choi, Y.H. Jo, S.S. Sohn, S. Lee, B.J. Lee, Understanding the physical metallurgy of the CoCrFeMnNi high-entropy alloy: an atomistic simulation study, *Npj Comput. Mater.* 2018 41. 4 (2018) 1–9. <https://doi.org/10.1038/s41524-017-0060-9>.
- [50] M. superlattices Yanli Zhang, G.-C. Wang, T.-M. Lu, al -, Y.-K. Kim, W.-S. Jung, B.-J. Lee, Modified embedded-atom method interatomic potentials for the Ni–Co binary and the Ni–Al–Co ternary systems, *Model. Simul. Mater. Sci. Eng.* 23 (2015) 055004. <https://doi.org/10.1088/0965-0393/23/5/055004>.
- [51] S.H. Oh, D. Seol, B.J. Lee, Second nearest-neighbor modified embedded-atom method interatomic potentials for the Co–M (M = Ti, V) binary systems, *Calphad.* 70 (2020) 101791. <https://doi.org/10.1016/J.CALPHAD.2020.101791>.
- [52] C. Wu, B.J. Lee, X. Su, Modified embedded-atom interatomic potential for Fe–Ni, Cr–Ni and Fe–Cr–Ni systems, *Calphad.* 57 (2017) 98–106. <https://doi.org/10.1016/J.CALPHAD.2017.03.007>.
- [53] Y.K. Kim, H.K. Kim, W.S. Jung, B.J. Lee, Development and application of Ni–Ti and Ni–Al–Ti 2NN-MEAM interatomic potentials for Ni-base superalloys, *Comput. Mater. Sci.* 139 (2017) 225–233. <https://doi.org/10.1016/J.COMMATSCI.2017.08.002>.
- [54] E. Lee, B.J. Lee, Modified embedded-atom method interatomic potential for the Fe–Al system, *J. Phys. Condens. Matter.* 22 (2010) 175702. <https://doi.org/10.1088/0953-8984/22/17/175702>.
- [55] I. Sa, B.J. Lee, Modified embedded-atom method interatomic potentials for the Fe–Nb and Fe–Ti binary systems, *Scr. Mater.* 59 (2008) 595–598. <https://doi.org/10.1016/J.SCRIPTAMAT.2008.05.007>.
- [56] J. Wang, H. Kwon, H.S. Kim, B.J. Lee, A neural network model for high entropy alloy design, *Npj Comput. Mater.* 2023 91. 9 (2023) 1–13. <https://doi.org/10.1038/s41524-023-01010-x>.
- [57] J. Zhang, S. Ma, Y. Xiong, B. Xu, S. Zhao, Elemental partitions and deformation mechanisms of L12-type multicomponent intermetallics, *Acta Mater.* 219 (2021) 117238. <https://doi.org/10.1016/J.ACTAMAT.2021.117238>.
- [58] P.M. Larsen, Sør. Schmidt, J. SchiØtz, Robust structural identification via polyhedral template matching, *Model. Simul. Mater. Sci. Eng.* 24 (2016) 055007. <https://doi.org/10.1088/0965-0393/24/5/055007>.

- [59] S.L. Ball, K.C. Alexander, C.A. Schuh, L. Yang, Z. Ma, A. Stukowski, Visualization and analysis of atomistic simulation data with OVITO—the Open Visualization Tool, *Model. Simul. Mater. Sci. Eng.* 18 (2009) 015012. <https://doi.org/10.1088/0965-0393/18/1/015012>.
- [60] T. Yang, Y.L. Zhao, Y. Tong, Z.B. Jiao, J. Wei, J.X. Cai, X.D. Han, D. Chen, A. Hu, J.J. Kai, K. Lu, Y. Liu, C.T. Liu, Multicomponent intermetallic nanoparticles and superb mechanical behaviors of complex alloys, *Science* (80-.). 362 (2018) 933–937. <https://doi.org/10.1126/science.aas8815>.
- [61] D. Chen, F. He, B. Han, Q. Wu, Y. Tong, Y. Zhao, Z. Wang, J. Wang, J. jung Kai, Synergistic effect of Ti and Al on L12-phase design in CoCrFeNi-based high entropy alloys, *Intermetallics*. 110 (2019) 106476. <https://doi.org/10.1016/J.INTERMET.2019.106476>.
- [62] Z.Y. Ding, B.X. Cao, J.H. Luan, Z.B. Jiao, Synergistic effects of Al and Ti on the oxidation behaviour and mechanical properties of L12-strengthened FeCoCrNi high-entropy alloys, *Corros. Sci.* 184 (2021) 109365. <https://doi.org/10.1016/J.CORSCI.2021.109365>.
- [63] Q. Gao, Y. Jiang, Z. Liu, H. Zhang, C. Jiang, X. Zhang, H. Li, Effects of alloying elements on microstructure and mechanical properties of Co–Ni–Al–Ti superalloy, *Mater. Sci. Eng. A.* 779 (2020) 139139. <https://doi.org/10.1016/J.MSEA.2020.139139>.
- [64] N.D. Stepanov, D.G. Shaysultanov, R.S. Chernichenko, M.A. Tikhonovsky, S. V. Zherebtsov, Effect of Al on structure and mechanical properties of Fe-Mn-Cr-Ni-Al non-equiatomic high entropy alloys with high Fe content, *J. Alloys Compd.* 770 (2019) 194–203. <https://doi.org/10.1016/J.JALLCOM.2018.08.093>.
- [65] Z. Sun, C. Shi, C. Liu, H. Shi, J. Zhou, The effect of short-range order on mechanical properties of high entropy alloy Al_{0.3}CoCrFeNi, *Mater. Des.* 223 (2022) 111214. <https://doi.org/10.1016/J.MATDES.2022.111214>.
- [66] S. Shen, Y. Li, L. Hao, X. Zhang, X. Liu, J. Du, M. Song, T. Shen, E. Fu, Ultrastrong and ductile FeNi-based alloys through Pd-containing multicomponent L12-type precipitates, *Mater. Des.* 244 (2024) 113112. <https://doi.org/10.1016/J.MATDES.2024.113112>.
- [67] H. Xie, Z. Ma, W. Zhang, H. Zhao, L. Ren, Strengthening effect of high-entropy alloys endowed by monolayer graphene, *Mater. Today Phys.* 27 (2022) 100800. <https://doi.org/10.1016/J.MTPHYS.2022.100800>.
- [68] X. Gao, J. Liu, W. Fu, Y. Huang, Z. Ning, Z. Zhang, J. Sun, W. Chen, Strong and ductile CoCrFeNi high-entropy alloy microfibers at ambient and cryogenic temperatures, *Mater. Des.* 233 (2023) 112250. <https://doi.org/10.1016/J.MATDES.2023.112250>.
- [69] J.P. Hirth, J. Lothe, T. Mura, *Theory of Dislocations* (2nd ed.), *J. Appl. Mech.* 50 (1983) 476–477. <https://doi.org/10.1115/1.3167075>.
- [70] A.J.E. Foreman, Dislocation energies in anisotropic crystals, *Acta Metall.* 3 (1955) 322–330. [https://doi.org/10.1016/0001-6160\(55\)90036-5](https://doi.org/10.1016/0001-6160(55)90036-5).
- [71] M.M. Savin, V.M. Chernov, A.M. Strokova, Energy factor of dislocations in hexagonal crystals, *Phys. Status Solidi.* 35 (1976) 747–754. <https://doi.org/10.1002/PSSA.2210350240>.
- [72] N. Ali, J. Li, L. Zhang, C. Zhang, H. Zhou, D. Liu, K. Sanaullah, Y. Nian, J. Cheng, Break the strength and ductility trade-off in novel NbC reinforced Fe_{40.5}(CoCr)₂₅Mn_{17.5}Ni₁₀Si₅ high entropy alloy, *Mater. Des.* 239 (2024) 112752. <https://doi.org/10.1016/J.MATDES.2024.112752>.
- [73] Y. Zhao, H. Ma, L. Zhang, D. Zhang, S. Kou, B. Wang, W. Li, P.K. Liaw, Mn content optimum on microstructures and mechanical behavior of Fe-based medium entropy alloys, *Mater. Des.* 223 (2022) 111241. <https://doi.org/10.1016/J.MATDES.2022.111241>.
- [74] Z. Pei, M. Eisenbach, P.K. Liaw, M. Chen, Nanoscale fluctuation of stacking fault energy strengthens multi-principal element alloys, *J. Mater. Sci. Technol.* 158 (2023) 218–225. <https://doi.org/10.1016/J.JMST.2023.01.042>.
- [75] T.H. Chou, W.P. Li, L.Y. Zhu, F. Zhu, X.C. Li, J. Huang, Y.X. Wang, R. Zhou, W.Y. Chen, J.H. Luan, Y.L. Zhao, Z.X. Wu, F.R. Chen, J.C. Huang, P.K. Liaw, X.L. Wang, T. Yang, *Critical*

- impacts of thermodynamic instability and short-range order on deformation mechanisms of VCoNi medium-entropy alloy, *Acta Mater.* (2024) 120190. <https://doi.org/10.1016/J.ACTAMAT.2024.120190>.
- [76] A. Saeed-Akbari, J. Imlau, U. Prahl, W. Bleck, Derivation and variation in composition-dependent stacking fault energy maps based on subregular solution model in high-manganese steels, *Metall. Mater. Trans. A Phys. Metall. Mater. Sci.* 40 (2009) 3076–3090. <https://doi.org/10.1007/s11661-009-0050-8>.
- [77] J.S. Jeong, W. Woo, K.H. Oh, S.K. Kwon, Y.M. Koo, In situ neutron diffraction study of the microstructure and tensile deformation behavior in Al-added high manganese austenitic steels, *Acta Mater.* 60 (2012) 2290–2299. <https://doi.org/10.1016/j.actamat.2011.12.043>.
- [78] Y. Zeng, X. Cai, M. Koslowski, Effects of the stacking fault energy fluctuations on the strengthening of alloys, *Acta Mater.* 164 (2019) 1–11. <https://doi.org/10.1016/J.ACTAMAT.2018.09.066>.
- [79] H. Li, H. Zong, S. Li, S. Jin, Y. Chen, M.J. Cabral, B. Chen, Q. Huang, Y. Chen, Y. Ren, K. Yu, S. Han, X. Ding, G. Sha, J. Lian, X. Liao, E. Ma, J. Sun, Uniting tensile ductility with ultrahigh strength via composition undulation, *Nat. 2022* 6047905. 604 (2022) 273–279. <https://doi.org/10.1038/s41586-022-04459-w>.
- [80] L. Proville, B. Bakó, Dislocation depinning from ordered nanophases in a model fcc crystal: From cutting mechanism to Orowan looping, *Acta Mater.* 58 (2010) 5565–5571. <https://doi.org/10.1016/J.ACTAMAT.2010.06.018>.
- [81] E. V. Fomin, A.E. Mayer, V.S. Krasnikov, Prediction of shear strength of cluster-strengthened aluminum with multi-scale approach describing transition from cutting to bypass of precipitates by dislocations, *Int. J. Plast.* 146 (2021) 103095. <https://doi.org/10.1016/J.IJPLAS.2021.103095>.